Macromolecules
ARTICLE

Macromolecules **2010**, *43*, 9899–9907 **9899**
DOI: 10.1021/ma101748c

Production of Porous Polymeric Films with Unimodal or Bimodal Pore-Size Distributions via Depressurization- and Photopolymerization-Induced Bubble Nucleation in Low-Viscosity UV-Curable Monomer/High-Pressure CO_2 Solutions

Kentaro Taki* and Shuhei Okumura

Department of Chemical Engineering, A4-021, Katsura Campus, Kyoto University, Katsura, Kyoto, 615-8510, Japan

Received August 10, 2010; Revised Manuscript Received October 16, 2010

ABSTRACT: The control of pore-size distribution in porous films is essential in many applications. Here, we report the development of a process facilitating the production of polymeric porous films with bimodal or unimodal pore-size distributions. High-pressure CO_2 was homogeneously dissolved into a liquid film comprised of a UV-curable monomer and a photoinitiator solution. The CO_2 pressure was released to atmospheric pressure, causing bubble nucleation via depressurization-induced phase separation. Simultaneously, UV light was applied to the film, causing bubble nucleation via photopolymerization-induced phase separation. During this time, the nucleated bubbles expanded and coalesced and the UV light induced the photopolymerization of the monomer. Photopolymerization solidified and stabilized the transient porous (bubble) structure of the thin film. Interestingly, the timing of the UV irradiation altered the pore-size distribution in the film. When UV irradiation was applied prior to depressurization-induced phase separation, most of the bubble nucleation occurred via photopolymerization-induced phase separation, and the pore-size distribution was unimodal, with a mean pore diameter of 10 μm. However, when the UV irradiation was applied after depressurization-induced phase separation, the pore size-distribution was bimodal, with two maxima at diameters of 10 and >20 μm, due to the dual modes of bubble nucleation (i.e., depressurization and photopolymerization) and subsequent bubble coalescence. This process facilitates the creation of films with either bimodal or unimodal pore-size distributions.

Introduction

Microporous polymeric films are used in a wide range of applications in which the pore-size distribution must be controlled, including electronics,[1] biomaterials,[2] membranes,[3−5] and optics.[6,7] Several methods have been developed to prepare microporous films, especially polymer membranes, utilizing phase separation, these include: nonsolvent-induced, evaporation-induced, vapor-induced and thermally induced methods.[8] Polymer foaming by depressurization-induced phase separation, i.e., the phase separation of a volatile liquid or gas from the polymer matrix, is a facile method for preparing closed-pore polymer foams and is widely used to produce commodity materials (e.g., heat insulation, packaging, and shock absorbers) and industrial goods (e.g., automobile interior fittings and ocean buoys).

The polymer foaming technique, or, more specifically, batch polymer foaming, has attracted the attention of many researchers since the microcellular plastic process was first developed.[9−15] This process consists of four steps: (1) the dissolution of a gas or volatile liquid at high pressure into a polymer; (2) depressurization to induce a metastable thermodynamic state; (3) depressurization-induced phase separation (DIPS) and the subsequent nucleation of gas bubbles from the polymer matrix; and (4) the expansion of the bubbles as the gas diffuses from the polymer matrix, leaving behind pores in the polymer matrix. Thermally induced phase separation (TIPS) occurs when some of the CO_2 gas remains in the polymer matrix after depressurization, and bubbles are nucleated by heating the sample.

Batch polymer-foaming techniques have been applied to both rubbery- and glassy- state polymers. The foaming of rubbery-state polymers can create films with micrometer-sized pores due to their high elasticity, which likely suppresses undesired bubble expansion and coalescence, and eventually stabilizes the porous structure at the micrometer size.

It is expected that a porous film cannot be created from a low-viscosity (elastic) liquid via polymer foaming. In such a case, bubble nucleation would be facilitated, but the bubbles would not retain their shape due to the low viscosity. To create a microporous film from a low-viscosity liquid, an instantaneous increase in elasticity and viscosity would be essential to stabilize the nucleated bubbles.

The photopolymerization of monomers, which causes the instantaneous polymerization and large increases in the viscosity and elasticity of the material, has been considered as an alternative technique to create porous structures from low-viscosity liquids and to control their pore-size distributions. The photopolymerization of UV-curable monomers and their phase separation have been extensively studied in the fields of photopolymerization-induced phase separation (PIPS) using liquid crystalline molecules and UV-curable monomers.[16−34] A homogeneous solution of liquid-crystalline molecules in a UV-curable monomer can undergo phase separation as a result of the heat of photopolymerization and polymerization itself. The size of the liquid-crystalline domain can be tuned to within the range $0.01-10$ μm by altering the photopolymerization rate, the monomer used, the volume fraction of liquid-crystalline molecules, the irradiation intensity, the initiator

*To whom all correspondence should be addressed . Telephone: +81-75-383-2696. Fax: +81-75-383-2696. E-mail: taki@cheme.kyoto-u.ac.jp..

Published on Web 11/04/2010

type, and the initiator concentration. Moreover, PIPS has been applied to prepare polymer blends with interpenetrating network (IPN) structures[35−37] and solvent foams.[38]

Polymer foaming generally creates a unimodal pore-size distribution. However, bimodal pore-size distributions in which smaller pores surround larger pores have been created in silica,[39−41] carbon[42] and other inorganic materials[43,44] with both micro- and mesopores and have subsequently been applied in catalysts, bioscaffolds and optics. Several methods have been investigated for creating bimodal pore-size distributions via polymer foaming. Among these methods, there are three different techniques currently used to reliably create bimodal pore-size distributions. The first technique involves controlling the bubble-nucleation period to create sequential foaming steps at different degrees of supersaturation.[45] The second technique involves the use of bubble-nucleation sites,[46] and the third relies on controlling coalescence.[47,48] These techniques have been applied only to glassy or rubbery state polymers and cannot be applied to create bimodal pore size distributions in low-viscosity liquid materials. Films with bimodal pore-size distributions that can be made from low-viscosity liquids are promising materials that could potentially replace inorganic-material with soft materials in many applications. Low-viscosity liquids such as UV-curable monomers are able to copolymerize with functional components at room temperature. Combining two or more monomers into a single composite may provide a pathway toward achieving new and highly tailorable properties by taking advantage of the distinct properties of each component in the blend.

In this study, we developed a process to create bimodal pore-size distributions in films made from a low-viscosity liquid solution of a UV-curable monomer with the aid of polymer-foaming technology and photopolymerization. PIPS was extended to a solution containing UV-curable monomers and CO_2 to create a porous film. UV light was applied to the solution of UV curable monomers and CO_2 to cause PIPS of CO_2 from the polymerized matrix. A bimodal pore-size distribution was intentionally created by controlling both DIPS and PIPS. This process facilitates the creation of films with either bimodal or unimodal pore-size distributions.

Materials and Methods

Materials. Two types of UV-curable monomers were supplied by TOAGOSEI CO., Ltd., Japan: a urethane diacrylate prepolymer (Aronix M-1100), the base prepolymer, and an *N*-vinylpyrrolidone monomer, the reactive diluent (Aronix M-150). The photoinitiator, 2,4,6-trimethylbenzoyl diphenyl phosphine oxide was supplied by Wako Pure Chemical Industries, Ltd., Japan. The prepolymer, reactive diluent and photoinitiator were mixed homogeneously at a weight ratio of 70/29/1 at 60 °C in a 30 mL amber vial. The solution was stabilized by adding 0.2 wt % diethylamine. All chemical regents were used as received. The complex viscosity of the solution, measured using a rheometer (Physica MCR 301, Anton-Paar), indicated that the solution behaved in a manner equivalent to a Newtonian fluid of 0.27 Pa·s in the strain-rate range from 1 to 100 rad/s. Carbon dioxide (Showa Tansan, Japan) of 99.9% purity was used.

UV Light Source. A UV light source (a MUV-202U 200-W mercury−xenon lamp, Moritex, Japan) equipped with a quartz light guide (Moritex, Japan) and a converging lens (ML-30, Moritex, Japan) was used for PIPS. The UV light was mounted 6 cm above the top window of the apparatus during the experiments in which the solution was exposed to UV light. The UV intensity was set at 55 mW/cm^2 by adjusting the aperture of the UV light source. During visual observations of the PIPS, the UV light guide was mounted at the side entry of the microscope. The UV light was sequentially reflected by a full-reflection mirror and a half-silvered mirror in the microscope to align the optical axis of the UV light with the optical axis of the visible light source coming through the sample. A halogen lamp (Olympus) was used as a visible light source behind the sample and was filtered to eliminate UV emissions using a 250-μm-thick Kapton film.

Real-time Fourier-transform infrared spectroscopy, a photo-differential scanning calorimeter, and a photorheometer were used along with a UV light source (OmniCure S2000 high-pressure 200-W mercury-vapor short arc lamp, EXFO, Mississaugua, Ontario, Canada) equipped with a liquid light guide and a band-pass filter (peak 365 nm, EXFO, Mississaugua, Ontario, Canada) to irradiate the monomer/initiator mixtures. UV light was applied at an intensity of 55 mW/cm^2 for 60 s for *in situ* characterization measurements.

The incident light intensity was monitored using a UV radiometer (UT-150, USHIO, Japan) with a maximum intensity at 365 nm prior to each characterization measurement.

Photopolymerization-Induced Phase Separation (PIPS) Apparatus. Figure 1 shows a cross-sectional view of the experimental apparatus used for PIPS. This apparatus was formerly used for the visual observation of batch polymer foaming, as previously described.[48−50] The apparatus consists of a stainless-steel body (Tama Seiki Kogyo, Japan), two cylindrical sapphire windows (thickness: 10 mm, diameter: 25 mm) supported by O-rings, a stainless steel C-shaped spacer, four cartridge heaters, a thermocouple connected to a temperature controller (Shimaden, Japan), a CO_2 pump (Nihon Seimitsu Kagaku, Japan), a pressure transducer (VALCOM, Japan), a pressure-buffer tank (500 mL, Swagelok), a chiller, a CO_2 cylinder, two valves and stainless-steel tubes and fittings.

To dispense the sample liquid with high reproducibility, the top sapphire window was placed on an electronic balance and 8 ± 0.3 mg of the viscous sample solution was dropped onto the center of the window. The window was turned over and then inserted into the stainless-steel body. The gap between the windows was fixed at 0.6 mm with a stainless-steel spacer. The sample drop contacted the bottom window, forming a cylindrical shape 4 mm in diameter and 0.6 mm high. Because CO_2 gas was diffused through the sides of the cylindrical sample, the diameter of the cylinder between the windows had to be held constant to obtain high reproducibility.

The apparatus was maintained at 60 °C throughout the experiments. After flushing the apparatus with CO_2, high-pressure CO_2 was dissolved into the sample at 12 MPa for 1 h. Next, the CO_2 pressure was reduced to atmospheric pressure at an initial depressurization rate of approximately 1.5 MPa/s by opening valve 2 while closing valve 1. The dissolved CO_2 became supersaturated, and CO_2 bubbles began to nucleate during depressurization. Simultaneously, UV light was applied to the sample for a given irradiation time and intensity at a specified pressure level in the apparatus. A customized LabVIEW (Version 8.5, National Instruments) program and an analogue/digital board (NI-6009, National Instruments) synchronized the timing of the UV irradiation at a given CO_2 pressure during depressurization.

The porous film formed using the apparatus was cryofractured in a liquid-nitrogen bath. The cross-section was coated with a thin gold layer. The porous structure was observed using scanning electron microscopy (Tiny-SEM, Technex Lab Co., Ltd.) and evaluated quantitatively using the image-processing software Image J (National Institutes of Health). To visualize bubble nucleation and growth, a high-speed digital camera (HAS-220, DITECT Japan) and a long-working-distance microscope (VQ-Z50, Keyence) equipped with a liquid light guide for the UV light source were used.

Real-Time Fourier-Transform Infrared Spectroscopy (Real-Time FT-IR). Real-time FT-IR spectroscopy (VERTEX 70, Bruker Optics, Germany) was used to monitor the polymerization kinetics. The optical bench was similar to that used in previous studies.[51−53] A horizontal-transmission accessory (HTA) was designed to enable the mounting of liquid samples

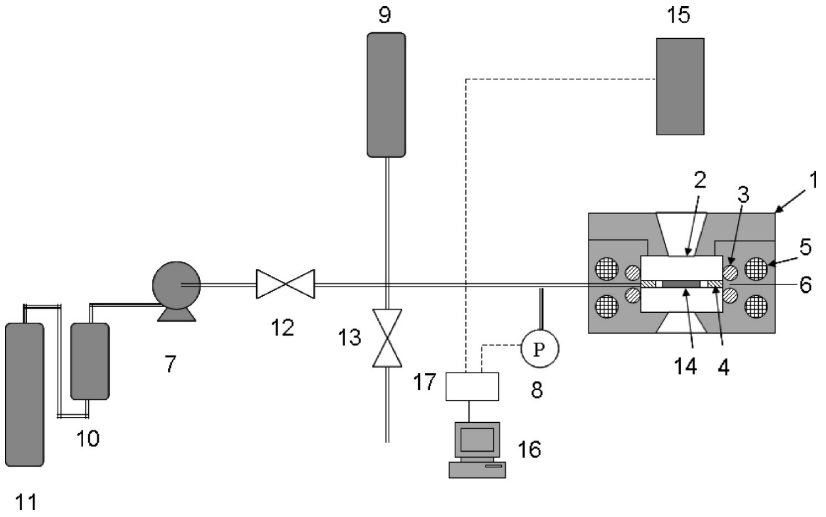

Figure 1. Experimental apparatus for photopolymerization-induced foaming. Key: (1) stainless steel body; (2) two cylindrical sapphire windows; (3) two O-rings; (4) stainless-steel spacer; (5) four cartridge heaters; (6) thermocouple; (7) CO_2 pump; (8) pressure transducer; (9) buffer tank; (10) chiller to liquefy CO_2; (11) CO_2 cylinder; (12) valve 1; (13) valve 2; (14) sample solution; (15) UV light source; (16) embedded personal computer with LabVIEW; (17) analog/digital board.

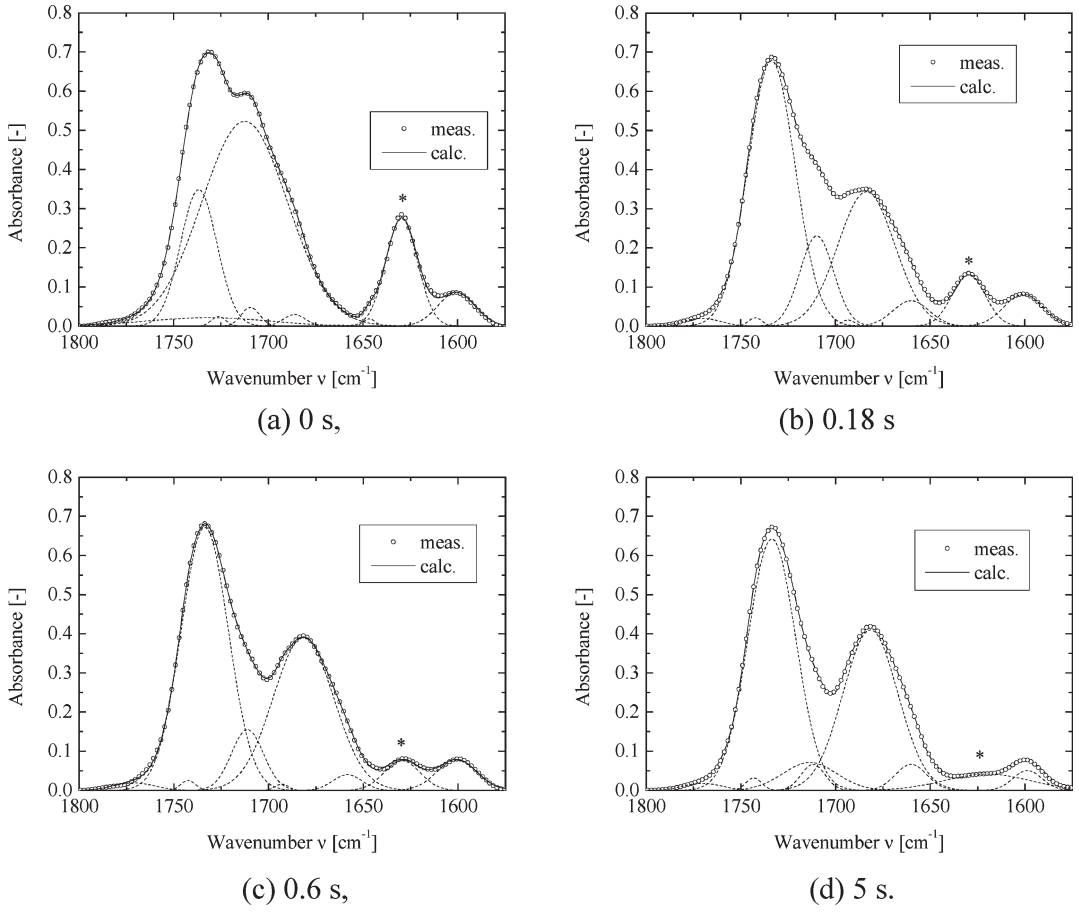

Figure 2. Peak deconvolution analysis of real-time FT-IR spectra obtained during the photopolymerization (UV intensity, 55 mW/cm^2; irradiation time, 60 s; sample thickness, 10 μm; sample holder temperature, 60 °C).

in a horizontal orientation for FT-IR measurements. A mercury cadmium telluride (MCT) detector and potassium bromide (KBr) coated beam splitter combination was used in conjunction with the rapid-scan option of the spectrometer to obtain a temporal resolution (33 ms) sufficient for monitoring the photopolymerization. The UV light source was located 3 cm above the sample. The sample stage was kept at 60 °C using a temperature-control device designed and constructed for use with a ceramic heater (Systems Engineering, Tokyo, Japan) in conjunction with the horizontal-transmission accessory. Samples (with a cured thickness of approximately 10 μm) were prepared by sandwiching a drop of the sample solution between two freshly cleaved KBr crystals (JASCO, Japan). The measurements were performed at 60 °C in a nitrogen atmosphere.

Each measured spectrum was processed using peak-deconvolution software developed in our laboratory. The software enabled us to extract the peak of the C=C group around 1,630 cm^{-1} from the measured spectra, which coupled with the C=O peaks of urethane diacrylate and *N*-vinylpyrrolidone. The software employed a couple of Gaussian functions and the nonlinear least-squares method in the MATLAB Optimization Toolbox. A peak height around 1630 cm^{-1} was used to quantify the amount of C=C group in a sample. The normalized absorbance was calculated by dividing each peak height by the peak height of the first spectrum. At least five measurements were carried out to ensure reproducibility.

Photorheometry. Photorheological measurements were carried out in a controlled-strain dynamic rotational rheometer (ARES, TA Instruments) with a 2-to-2000 g·cm force-rebalance transducer and a UV light guide. This measurement apparatus was developed based on previous studies.[54,55] An upper fixture allowed the coupling of the UV light source to an upper sapphire plate and enabled the passage of UV light. The sample was inserted between the sapphire plate and a parallel stainless steel plate, both of which had a diameter of 20 mm. The stainless steel bottom plate was maintained at 60 °C by water circulation. The dynamic time-sweep test mode with the fast-sampling option in the ARES software (Orchestrator, TA Instruments) was used to monitor the changes in viscoelastic behavior during photopolymerization. The frequency and strain were 1 rad/s and 1%, respectively. The sample thickness was 0.60 mm.

Photodifferential Scanning Calorimeter (Photo-DSC) Measurement. The photo-DSC apparatus and the data processing of the photo-DSC profiles were based on a previous study.[56] The isothermal heat of photopolymerization was monitored using a DSC (DSC8500, Perkin-Elmer, USA) with a cooling accessory able to decrease the temperature to −100 °C. For the photo-DSC measurements, the DSC instrument was upgraded to allow for the UV irradiation of the sample and reference pans using a bifurcated fiber-optic lead, thus minimizing the thermal heating effect of the UV light source. The fiber was mounted on a metal fixture on the DSC cover. The DSC cover and furnace were flushed with 20 mL/min of nitrogen gas (99.998%). The metal fixture was heated to 35 ± 1 °C to avoid the accumulation of condensation from the air. Two DSC runs were performed for every sample to minimize the effect of radiant heat from the UV source. The first heat-flow profile, which included the heat of photopolymerization and the radiant heat, was subtracted from the second heat-flow profile, which included only the radiant heat. Measurements were performed at an isothermal condition of 60 °C.

Real-time FT-IR, photorheometry, and photo-DSC measurements were performed under ambient pressure. The sample solution was homogeneously cured, indicating that PIPS was not observed.

Results and Discussion

Figure 2 shows the results of the peak deconvolution analysis. The absorbance was calculated for each wavenumber by the summation of the peaks represented by dashed lines. Almost all of the calculated spectra agree well with the experimental spectra. Figure 2a, which shows the spectrum measured before photopolymerization, indicates that four large peaks and five small peaks of the Gaussian function are necessary to reproduce the measured spectrum. The peak of the C=C group at 1630 cm^{-1} indicated as "∗", was clearly extracted by the analysis. Comparing the heights around 1630 cm^{-1} in Figure 2, parts a−d, the peak height around 1630 cm^{-1} decreases with time as the polymerization occurred.

Figure 3 shows the change in the normalized absorbance of the C=C group at 1,630 cm^{-1}, as measured using real-time FT-IR. When irradiated with UV light, the normalized absorbance instantaneously started to decrease. Within 1.0 s, the normalized absorbance became 0.22, which means 78% of the monomers had cured.

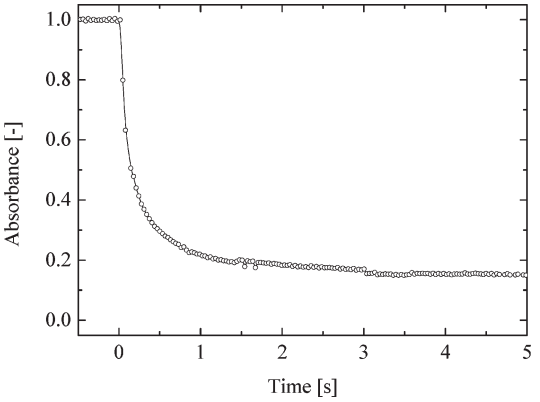

Figure 3. Real-time FT-IR measurement of the photopolymerization of the monomers by UV irradiation (UV intensity, 55 mW/cm^2; irradiation time, 60 s; sample thickness, 10 μm; sample holder temperature, 60 °C).

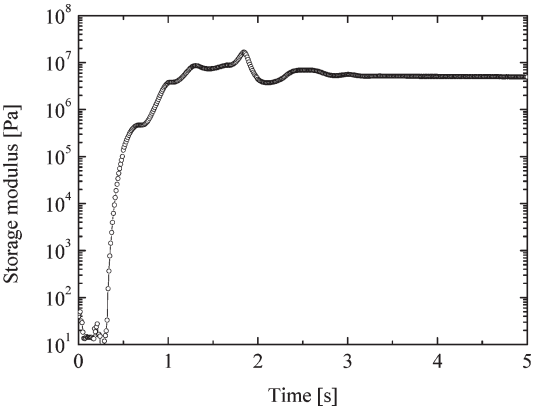

Figure 4. Change in the storage modulus during photopolymerization (UV intensity at 365 nm, 55 mW/cm^2; irradiation time, 60 s; sample thickness, 0.6 mm).

Figure 4 shows the change in the storage modulus during photopolymerization. In this study, the change in storage modulus, which is the stored elastic energy of a viscoelastic materials, represents how fast the sample was hardened during photopolymerization. The initial storage modulus was on the order of 10 Pa. When the sample was irradiated with UV light, a 0.4-s induction time was observed and then the storage modulus rapidly increased to over 10^6 Pa. Thus, the storage modulus increased 5 orders of magnitude within 1 s. The sample solution was cured as fast as in a previous study that used a urethane diacrylate formulation.[57]

To clarify the relationship between the conversion of the C=C group and the storage modulus, the conversion was calculated by subtracting the normalized absorbance in Figure 3 from unity. Because the data-acquisition period of the real-time FT-IR was shorter than that of the photorheometer, the conversion value corresponding to each storage-modulus point was calculated by interpolating between the two nearest conversion values. Figure 5 shows the relationship between the conversion and the storage modulus during photopolymerization. The storage modulus gradually decreased up to a conversion of 0.6 because the solution temperature was increased due to the heat of polymerization. The time required to reach a conversion of 0.6 was 0.26 s, as shown in Figure 3; the storage modulus then increased dramatically with conversion.

Figure 6 shows the heat of polymerization during photopolymerization. The DSC profile shows a negative peak, indicating that an exothermic photopolymerization reaction occurred. The

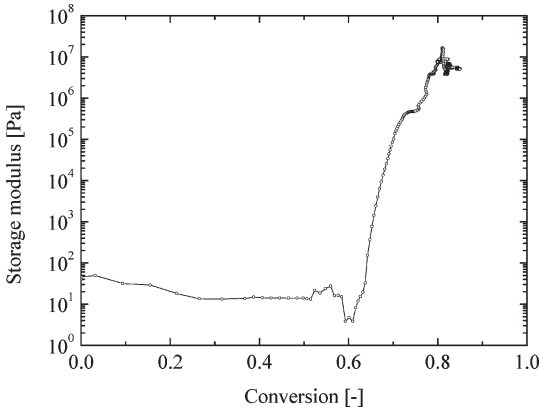

Figure 5. Conversion versus storage modulus during photopolymerization.

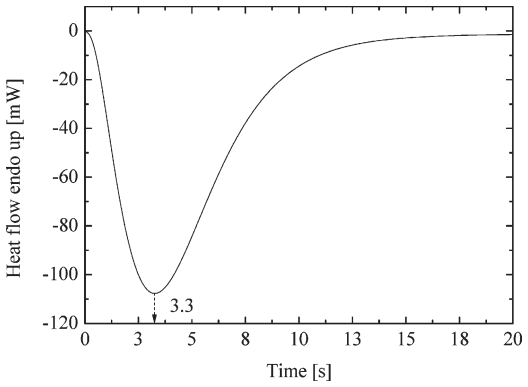

Figure 6. Heat of photopolymerization of the monomers by UV irradiation (UV intensity, 55 mW/cm^2; irradiation time, 60 s; sample weight, 0.7 mg).

heat flow reached a minimum value at 3.3 s. Because the DSC has a relatively long response time (2 s)[58] and the measurement had to be performed under isothermal conditions, the reaction appears to occur later than when observed by real-time FT-IR and photorheometer. The reader is referred to the Appendix for details of the temperature calculation from the heat flow, indicating that the sample temperature likely increased to over 110 °C during the reaction in the high-pressure apparatus during PIPS experiments.

Figure 7 shows the decrease in CO_2 pressure in the apparatus along with the time to the induction of bubble nucleation via DIPS. It took 20 s to decrease the pressure from 12 to 5.8 MPa in the apparatus. The irradiation pressure drop, ΔP_{ir}, superimposed on the pressure profile is defined here as the difference between the saturation pressure and the pressure at which the UV irradiation was applied.

Figure 8 shows a series of micrographs depicting bubble nucleation, growth and coalescence during DIPS without UV irradiation performed along the pressure profile indicated by the thick line in Figure 7. The time, pressure, and ΔP below each micrograph indicate the time after the onset of the CO_2 pressure release, the pressure in the high-pressure apparatus and the difference from saturation pressure, respectively. The micrograph taken at 0 s shows the initial condition of the sample solution when saturated with CO_2. The micrograph taken at 0.28 s and a pressure of 11.4 MPa shows a number of black dots that make a part of the micrograph turbid. These black dots were assumed to be CO_2 bubbles nucleated by DIPS. Although the bubble nuclei, at ~10 nm, could not be observed with the optical microscope, it was concluded that the true critical pressure for bubble nucleation induced by DIPS was a little higher than 11.4 MPa. For the sake of

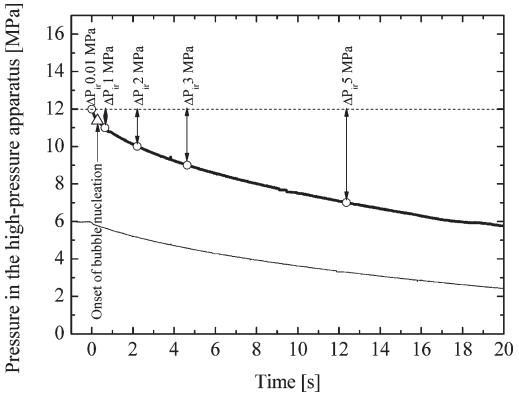

Figure 7. CO_2 pressure profiles in the apparatus. Thick line: pressure profile in the high-pressure apparatus used for Figure 8 and Figure 10; open circles: ΔP_{ir}; irradiation pressure drop; triangle: the observed onset of bubble nucleation. Thin line: pressure profile in the high-pressure apparatus for visual observation experiments with photopolymerization; see Figure 9.

simplicity, the critical pressure difference was taken as 0.6 MPa (=12.0−11.4 MPa). The triangle symbol in Figure 7 indicates the time and pressure in the high-pressure apparatus for which the onset of bubble nucleation induced via DIPS was observed, as shown in Figure 8. In the micrograph taken at 0.64 s, the number of bubbles has increased and the bubble diameter has increased to 12 μm. In the micrograph taken at 2.20 s, the bubble-diameter distribution has broadened. Because the complex viscosity of the sample was 0.27 Pa·s, the bubbles instantaneously coalesced upon collision, broadening the diameter distribution. Bubble coalescence and expansion continued, as shown in the micrograph taken at 4.63 s. The average bubble diameter increased to more than 200 μm, as shown in the micrograph taken at 12.4 s, a value calculated from the bubble curvature.

Figure 9 shows the bubble nucleation and growth caused by PIPS. To observe the bubble nucleation caused by PIPS, the CO_2 pressure was set at 6 MPa and a lower UV light intensity was used (1.5 mW/cm^2) to decrease the number of bubbles nucleated via PIPS. The UV irradiation time was 1.0 s. The time, pressure, and ΔP below each micrograph indicate the time after the onset of CO_2-pressure release, the pressure in the high-pressure apparatus and the difference from saturation pressure, respectively. The thinner curve in Figure 7 shows the pressure profile of the visually observed PIPS experiment.

No bubbles were nucleated by DIPS prior to irradiation (see Figure 9a). Applying UV irradiation made the background brighter, as shown in Figure 9b. At 0.4 s (= 3.3−2.9 s) s after initiation of the UV irradiation, the first bubble nucleated via PIPS appears at the bottom left of Figure 9c (indicated by an arrow). From the micrographs in Figure 9d−f, it is clear that the number of bubbles increased with UV irradiation time and depressurization. Depressurization-induced phase separation was also performed in a separate trial at the same saturation pressure without UV irradiation, verifying that no bubbles were nucleated without UV irradiation when the CO_2 pressure in the apparatus was less than 1 MPa (data not shown).

Prior to DIPS, the CO_2 molecules were dissolved in the UV-curing monomer solution at the saturation concentration at the given pressure and temperature (i.e., the equilibrium concentration of CO_2). After releasing the CO_2 pressure, the CO_2 solubility decreased with the decreasing pressure. The degree of CO_2 supersaturation increased as the difference between the CO_2 concentration and its solubility increased. At a certain degree of supersaturation, the dissolved CO_2 molecules nucleated as bubbles via DIPS.

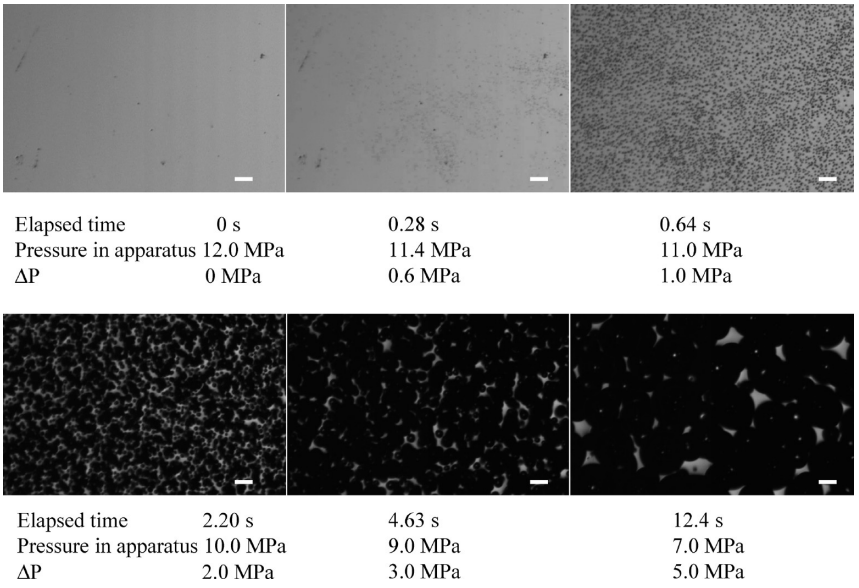

Figure 8. Micrographs of bubble nucleation, growth and coalescence via depressurization-induced phase separation (DIPS) in monomer/CO_2 solutions (scale bar, 100 μm; saturation pressure, 12 MPa; temperature, 60 °C).

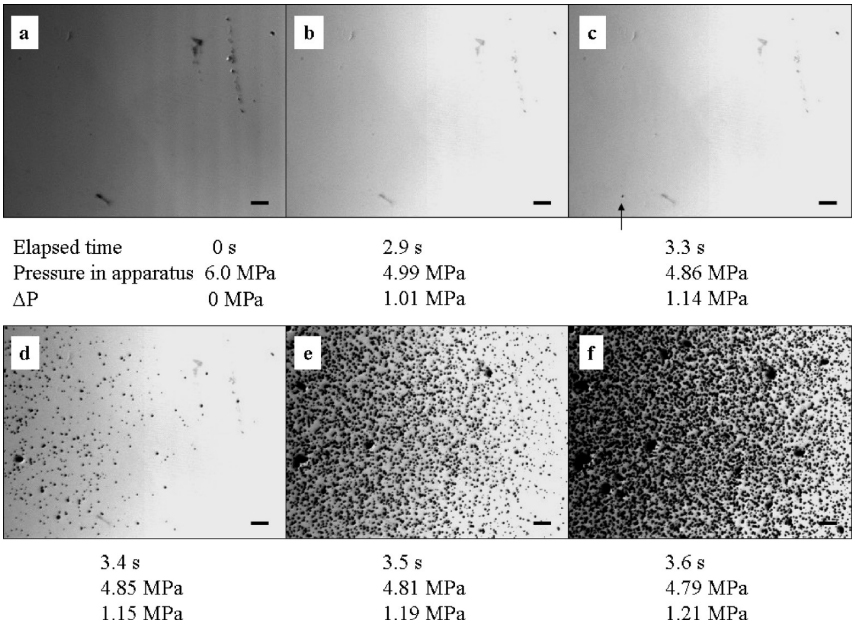

Figure 9. Visual observation of bubble nucleation, growth and coalescence via photopolymerization-induced phase separation (PIPS) in a monomer/CO_2 solution (pressure, 6 MPa; temperature, 60 °C; UV intensity, 1.5 mW/cm^2; irradiation time, 1.0 s; frame size, 1.2 × 1.6 mm; micrographs were taken every 0.025 s from micrograph c to i and 0.445 s elapsed from micrographs b to c). Scale bar: 100 μm.

The photopolymerization reaction used in this study was an exothermic radical polymerization, as shown in Figures 6 above and in Figure 13 of the Appendix; thus, the solution temperature may have increased during the reaction. No measurements of CO_2 solubility in urethane diacrylate and *N*-vinylpyrrolidone were found in the literature. However, Sato et al. reported that the solubility of high-pressure CO_2 in polypropylene, high-density polyethylene, and polystyrene decreased with increasing temperature.[59] They concluded that the temperature dependence of the Henry's Law constant for CO_2 is dominated by CO_2 gas condensation, indicating that the CO_2 solubility in polymers decreases with increased temperature at a given CO_2 pressure. It is thought that the increased solution temperature caused by photopolymerization decreased the CO_2 solubility and increased the degree of CO_2 supersaturation, adding to the effect of depressurization. As a result, bubbles could be nucleated at a lower critical pressure difference than was possible with DIPS only. The bubbles were thus likely nucleated by a combination of two different sources of supersaturation: depressurization-induced (DIPS) and photopolymerization-induced (PIPS) phase separation.

To characterize the effects of the two different bubble-nucleating mechanisms (i.e., DIPS and PIPS) on the porous structure, the irradiation pressure drop was varied from 0.01 to 10 MPa. The pressure profile in the high-pressure apparatus show in Figure 7 was used when reducing the CO_2 pressure; here, the irradiation pressure drop and the critical pressure difference are superimposed on the CO_2 pressure profile.

Figure 10 shows SEM micrographs of porous films obtained via DIPS and PIPS. Uniform pore-size distributions were obtained at

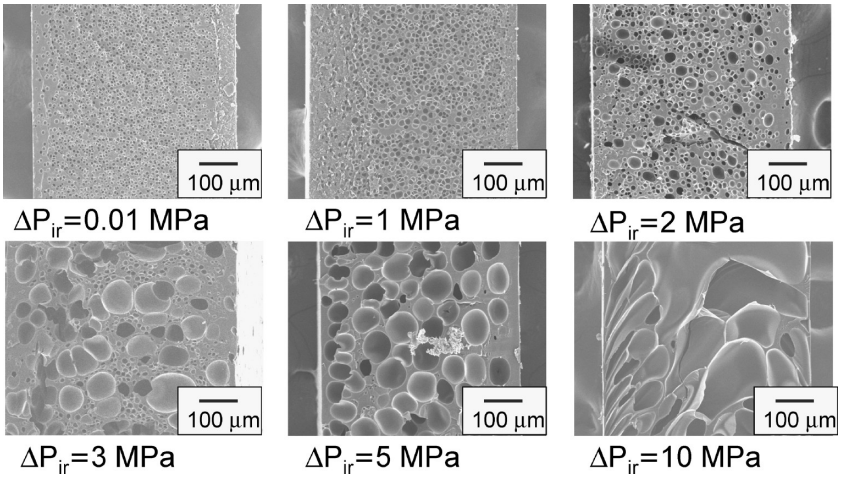

Figure 10. SEM micrographs showing effects of the irradiation pressure drop, ΔP_{ir}, on the porous structures prepared via depressurization-induced phase separation (DIPS) and photopolymerization-induced phase separation (PIPS) (saturation pressure, 12 MPa; temperature, 60 °C; UV intensity, 55 mW/cm^2; irradiation time, 60 s).

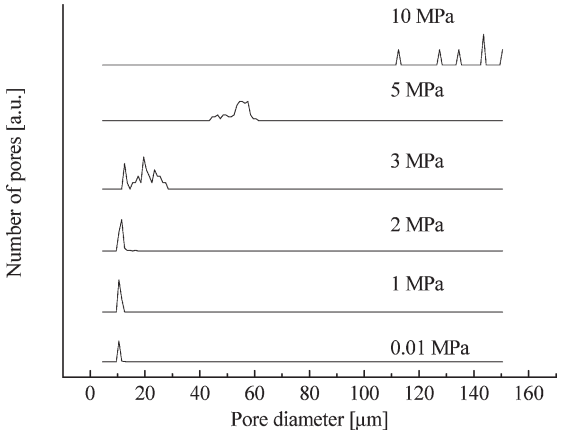

Figure 11. Effect of the irradiation pressure drop, ΔP_{ir}, on pore-size distribution via depressurization-induced phase separation (DIPS) and photopolymerization-induced phase separation (PIPS).

0.01 and 1 MPa irradiation pressure drops. However, bimodal pore-size distributions were obtained at 2 and 3 MPa. The pore-size distribution became unimodal again at 5 and 10 MPa. Almost all of the pores were closed. The pore-size distribution is quantitatively shown in Figure 11.

The ΔP_{ir} of 0.01 MPa is smaller than the critical pressure difference of 0.6 MPa for DIPS evident in Figure 8. The pores formed in experiments with a ΔP_{ir} of 0.01 MPa were therefore formed by the bubble nucleation induced by PIPS.

The ΔP_{ir} of 1 MPa was larger than the critical pressure difference of 0.6 MPa so, in this case, bubble nucleation was likely induced by both DIPS and PIPS. When the photopolymerization exceeded 60% conversion, the storage modulus increased to over 10^6 Pa. The time required to reach a conversion of 60% was 0.15 s, as shown in Figures 3 and 5. Because the photopolymerization was so rapid, the bubbles did not coalesce to any degree. Moreover, the decrease in the CO_2 concentration of the solution was small because the bubbles had just nucleated and there was insufficient time for CO_2 gas to diffuse into the bubbles. Thus, there were enough CO_2 molecules remaining in the solution to allow PIPS-based nucleation to occur between the bubbles generated by DIPS.

At ΔP_{ir} values of 2 and 3 MPa, as shown in Figure 8, the bubbles from DIPS had already coalesced, and the size distribution was thus broadened prior to UV irradiation. As with the ΔP_{ir} of 1 MPa, photopolymerization stabilized the porous structure and induced bubble nucleation by PIPS between the bubbles nucleated by DIPS. The larger pores originated from the depressurization, and the smaller pores were formed due to the polymerization.

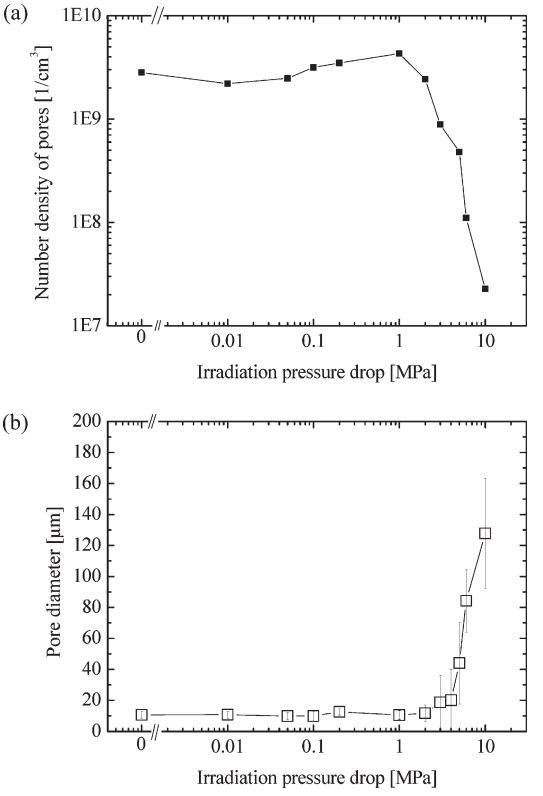

Figure 12. Effect of the irradiation pressure drop, ΔP_{ir}, on the pore-number density (a) and pore diameter (b) (saturation pressure, 12 MPa; temperature, 60 °C; UV intensity, 55 mW/cm^2; irradiation time, 60 s).

At a ΔP_{ir} value of 5 and 10 MPa, bubble nucleation occurred via DIPS; PIPS did not occur, even with UV irradiation. The nucleated bubbles consumed the dissolved CO_2 as they expanded and the concentration of CO_2 in the solution was below the level necessary for PIPS to occur. In this case, the main effect of the photopolymerization was to stabilize the porous structure.

Figure 12a shows the pore-number densities of the materials as determined by image analysis of the micrographs in Figure 10.

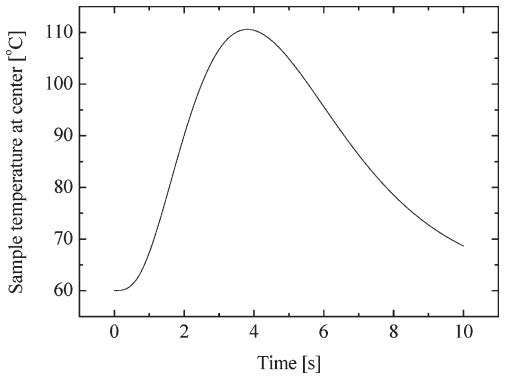

Figure 13. Change in sample temperature at the center (ρ = 1000 kg/m^3, C_p = 1900 J/(kg K), k = 0.12 W/(m K), L = 0.6 mm, T_0 = 333 K, w_g = 0.7 mg).

Note that the largest pore density was obtained at 1 MPa, indicating that the bubble-nucleation rate was greatest at the irradiation pressure drop of 1 MPa. The degree of supersaturation for the bubble nucleation via DIPS at 1 MPa was close to the critical level (0.6 MPa). In other words, the solution was irradiated near the critical point of supersaturation. When the UV light was irradiated at 10 MPa (ΔP_{ir}, 1 MPa), further bubble nucleation via PIPS occurred. Overall, the maximum bubble nucleation, which was the sum of that caused by DIPS and PIPS, was obtained with a pressure drop of 1 MPa.

As shown in Figure 8, the bubbles coalesced instantaneously when they came into contact. Eventually, the bubble diameter was more than 200 μm when no UV irradiation was used. However, as shown in Figure 12b, the size of the pores (bubbles) formed from ΔP_{ir} value of 1 to 4 MPa was between 10 and 20 μm, much smaller than the pores shown in Figure 8. This size difference clearly indicates that a rapid photopolymerization leads to a correspondingly rapid increase in viscosity and elasticity, which retards bubble growth and suppresses bubble coalescence, thus producing a smaller pore size. In other words, photopolymerization "froze" the transient porous structure forming in the solution.

Conclusions

We developed a process that facilitates the production of polymeric porous films with bimodal or unimodal pore-size distributions. DIPS- and PIPS-induced bubble nucleation in a UV-curable monomer/prepolymer solution with dissolved CO_2 was found to create closed-pore films. UV irradiation controlled the bimodal or unimodal nature of the porous structure. When UV irradiation was applied prior to bubble nucleation by DIPS, the resulting porous structure had a unimodal pore-size distribution. However, a bimodal porous structure was formed when UV irradiation was applied during the depressurization-induced bubble nucleation. The majority of the pores originated from the coalescence of bubbles resulting from DIPS, whereas the smaller pores located around the larger pores originated from PIPS.

The viscosity of the sample solution was too low to retain the porous structure without UV irradiation. When UV irradiation was applied to a sample solution containing a number of bubbles, the photopolymerization increased the elasticity of the sample solution and stabilized the transient porous structure.

The process developed herein allows for the production of bimodal porous films containing pores from 10 μm in diameter and to pores of over 20 μm, which are not particularly small compared to inorganic porous materials that have a single size of micro- to meso-sized pores as described in the Introduction. A further goal of this research will be to decrease the pore sizes to mesopore size and smaller by employing more rapidly curing UV-curable monomers to "freeze" the transient porous structure of the bubble nuclei.

Acknowledgment. The authors gratefully acknowledge Professor Emeritus Fumimaru Ogino, Professor Masahiro Ohshima, and Dr. Shinsuke Nagamine for their helpful discussion and Mr. Tomiya Abe for introducing us to the field of photopolymerization. This study was supported by the New Energy and Industrial Technology Development Organization, Japan (NEDO, 09A16003d).

Appendix

During the photopolymerization, the temperature of the sample solution would be expected to increase significantly because the exothermic reaction occurred in a few seconds. A numerical calculation was employed to estimate the temperature change during PIPS. The sample solution in the high-pressure apparatus was of a flat cylindrical shape, 4 mm in diameter and 0.6 mm thick. As the diameter of the sample cylinder was 6.7 times larger than its thickness, the temperature profile was calculated along the vertical axis. For simplicity's sake, it was assumed that solution density, ρ, thermal conductivity, k, and heat capacity, C_p, were all constant. The one-dimensional equation for energy with chemical reaction is as follows:[60]

$$\rho C_p \frac{\partial T}{\partial t} = k\frac{\partial^2 T}{\partial z^2} + q(t) \tag{1}$$

where T is temperature, t is time, and $q(t)$ is the heat-generation rate in a unit volume [W/m^3]. The heat-generation rate, $q(t)$, was calculated from the heat flow, $Q(t)$, measured using the photo-DSC as follows:

$$q(t) = Q(t)\frac{\rho}{m} \tag{2}$$

where m is sample mass in the photo-DSC measurement. It was assumed that the heat was generated in the sample solution uniformly. The boundary condition at the midline of the sample thickness is expressed by eq 3. As the thermal conductivity of sapphire was 350 times larger than the sample solution, heat generated may have been conducted through the sapphire window. The boundary condition, giving the fastest heat loss rate through the sapphire window at the boundary between the sample and the sapphire window, is described by eq 4.

$$\left.\frac{\partial T}{\partial z}\right|_{L=0} = 0 \tag{3}$$

$$T(t, L/2) = T_0 \tag{4}$$

where L is the sample thickness and T_0 is the initial temperature. Equations 1−4 were solved numerically using the explicit finite-difference method.

The calculated results for the time evolution of temperature rise at the center of the sample cylinder are shown in Figure 13. The sample temperature increased to over 110 °C with time. As photo-DSC has a slower response time than FT-IR and the photopolymerization reaction occurred under isothermal conditions, the actual temperature increase due to the PIPS in the sample in the high-pressure apparatus would be faster than the calculated result. Therefore, the calculated result suggests that at least a 50 °C rise was caused by the photopolymerization. Because the heat-generation rate of photopolymerization was faster than the heat loss through the sapphire windows, the system approximates adiabatic conditions.

References and Notes

(1) Ren, Y.; Lam, D. C. C. *J. Electron. Mater*. **2008**, *37*, 955–961.
(2) Tai, H. Y.; Mather, M. L.; Howard, D.; Wang, W. X.; White, L. J.; Crowe, J. A.; Morgan, S. P.; Chandra, A.; Williams, D. J.; Howdle, S. M.; Shakesheff, K. M. *Eur. Cells Mater*. **2007**, *14*, 64–76.
(3) Wu, Y. H.; Liu, Y. L.; Chang, Y.; Higuchi, A.; Freeman, B. D. *J. Membr. Sci*. **2010**, *348*, 47–55.
(4) Wu, Y. H.; Park, H. B.; Kai, T.; Freeman, B. D.; Kalika, D. S. *J. Membr. Sci*. **2010**, *347*, 197–208.
(5) Wu, Y. H.; Freeman, B. D. *J. Membr. Sci*. **2009**, *344*, 182–189.
(6) Seo, J. H.; Cha, S. W.; Kim, H. B. *J. Polym. Eng*. **2009**, *29*, 79–102.
(7) Mitrofanov, A. V.; Apel, P. Y.; Blonskaya, I. V.; Orelovitch, O. L. *Technical Physics* **2006**, *51*, 1229–1234.
(8) He, D.; Susanto, H.; Ulbricht, M. *Prog. Polym. Sci*. **2009**, *34*, 62–98.
(9) Colton, J. S.; Suh, N. P. *Polym. Eng. Sci*. **1987**, *27*, 500–503.
(10) Colton, J. S.; Suh, N. P. *Polym. Eng. Sci*. **1987**, *27*, 485–492.
(11) Colton, J. S.; Suh, N. P. *Polym. Eng. Sci*. **1987**, *27*, 493–499.
(12) Krause, B.; Mettinkhof, R.; van der Vegt, N. F. A.; Wessling, M. *Macromolecules* **2001**, *34*, 874–884.
(13) Kumar, V.; Suh, N. P. *Polym. Eng. Sci*. **1990**, *30*, 1323–1329.
(14) Stafford, C. M.; Russell, T. P.; McCarthy, T. J. *Macromolecules* **1999**, *32*, 7610–7616.
(15) Taki, K.; Waratani, Y.; Ohshirna, M. *Macromol. Mater. Eng*. **2008**, *293*, 589–597.
(16) Artal, C.; Ros, M. B.; Serrano, J. L.; Pereda, N.; Etxebarria, J.; Folcia, C. L.; Ortega, J. *Macromolecules* **2001**, *34*, 4244–4255.
(17) Bhargava, R.; Wang, S. Q.; Koenig, J. L. *Macromolecules* **1999**, *32*, 8982–8988.
(18) Clapper, J. D.; Guymon, C. A. *Macromolecules* **2007**, *40*, 7951–7959.
(19) Guymon, C. A.; Bowman, C. N. *Macromolecules* **1997**, *30*, 5271–5278.
(20) Guymon, C. A.; Bowman, C. N. *Macromolecules* **1997**, *30*, 1594–1600.
(21) Kyu, T.; Nwabunma, D. *Macromolecules* **2001**, *34*, 9168–9172.
(22) Meng, S.; Duran, H.; Hu, J.; Kyu, T.; Natarajan, L. V.; Tondiglia, V. P.; Sutherland, R. L.; Bunning, T. J. *Macromolecules* **2007**, *40*, 3190–3197.
(23) Meng, S.; Kyu, T.; Natarajan, L. V.; Tondiglia, V. P.; Sutherland, R. L.; Bunning, T. J. *Macromolecules* **2005**, *38*, 4844–4854.
(24) Nwabunma, D.; Chin, H. W.; Kyu, T. *Macromolecules* **2000**, *33*, 1416–1424.
(25) Nwabunma, D.; Kim, K. J.; Lin, Y. H.; Chien, L. C.; Kyu, T. *Macromolecules* **1998**, *31*, 6806–6812.
(26) Ozawa, J.; Matsuo, G.; Kamo, N.; Tsujii, K. *Macromolecules* **2006**, *39*, 7998–8002.
(27) Park, S. J.; Kyu, T. *Macromolecules* **2009**, *42*, 1180–1188.
(28) Roper, T. M.; Lee, T. Y.; Guymon, C. A.; Hoyle, C. E. *Macromolecules* **2005**, *38*, 10109–10116.
(29) Serbutoviez, C.; Kloosterboer, J. G.; Boots, H. M. J.; Touwslager, F. J. *Macromolecules* **1996**, *29*, 7690–7698.
(30) Tan, C. B.; Sun, H.; Fung, B. M.; Grady, B. P. *Macromolecules* **2000**, *33*, 6249–6254.
(31) Trajkovska, A.; Kim, C.; Marshall, K. L.; Mourey, T. H.; Chen, S. H. *Macromolecules* **2006**, *39*, 6983–6989.
(32) Trollsas, M.; Sahlen, F.; Gedde, U. W.; Hult, A.; Hermann, D.; Rudquist, P.; Komitov, L.; Lagerwall, S. T.; Stebler, B.; Lindstrom, J.; Rydlund, O. *Macromolecules* **1996**, *29*, 2590–2598.
(33) White, T. J.; Natarajan, L. V.; Tondiglia, V. P.; Bunning, T. J.; Guymon, C. A. *Macromolecules* **2007**, *40*, 1112–1120.
(34) White, T. J.; Natarajan, L. V.; Tondiglia, V. P.; Lloyd, P. F.; Bunning, T. J.; Guymon, C. A. *Macromolecules* **2007**, *40*, 1121–1127.
(35) Murata, K.; Amamiya, A.; Anazawa, T. *Macromol. Mater. Eng*. **2003**, *288*, 58–65.
(36) Murata, K.; Anazawa, T. *Polymer* **2002**, *43*, 6575–6583.
(37) Murata, K.; Sachin, J.; Etori, H.; Anazawa, T. *Polymer* **2002**, *43*, 2845–2859.
(38) Apen, P. G. *J. Cellular Plast* **1995**, *31*, 74–92.
(39) Lebeau, B.; Fowler, C. E.; Mann, S.; Farcet, C.; Charleux, B.; Sanchez, C. *J. Mater. Chem*. **2000**, *10*, 2105–2108.
(40) Antonietti, M.; Berton, B.; Goltner, C.; Hentze, H. P. *Adv. Mater*. **1998**, *10*, 154–159.
(41) Mishra, S.; Mitra, R. *J. Mater. Sci*. **2010**, *45*, 4115–4125.
(42) Deng, Y. H.; Liu, C.; Yu, T.; Liu, F.; Zhang, F. Q.; Wan, Y.; Zhang, L. J.; Wang, C. C.; Tu, B.; Webley, P. A.; Wang, H. T.; Zhao, D. Y. *Chem. Mater*. **2007**, *19*, 3271–3277.
(43) Schmidt, H.; Koch, D.; Grathwohl, G.; Colombo, P. *J. Am. Ceram. Soc*. **2001**, *84*, 2252–2255.
(44) Marques, A. C.; Jain, H.; Almeida, R. M. *Phys. Chem. Glasses: Eur. J. Glass Sci. Technol., Part B* **2007**, *48*, 65–68.
(45) Arora, K. A.; Lesser, A. J.; McCarthy, T. J. *Macromolecules* **1998**, *31*, 4614–4620.
(46) Siripurapu, S.; DeSimone, J. M.; Khan, S. A.; Spontak, R. J. *Macromolecules* **2005**, *38*, 2271–2280.
(47) Yokoyama, H.; Sugiyama, K. *Macromolecules* **2005**, *38*, 10516–10522.
(48) Taki, K.; Nitta, K.; Kihara, S.; Ohshima, M. *J. Appl. Polym. Sci*. **2005**, *97*, 1899–1906.
(49) Taki, K.; Nakayama, T.; Yatsuzuka, T.; Ohshima, M. *J. Cellular Plast*. **2003**, *39*, 155–169.
(50) Taki, K.; Yanagimoto, T.; Funami, E.; Okamoto, M.; Ohshima, M. *Polym. Eng. Sci*. **2004**, *44*, 1004–1011.
(51) Berchtold, K. A.; Nie, J.; Stansbury, J. W.; Bowman, C. N. *Macromolecules* **2008**, *41*, 9035–9043.
(52) Decker, C.; Moussa, K. *Macromolecules* **1989**, *22*, 4455–4462.
(53) Decker, C. *Macromol. Rapid Commun*. **2002**, *23*, 1067–1093.
(54) Lee, S. S.; Luciani, A.; Manson, J. A. E. *Prog. Org. Coat*. **2000**, *38*, 193–197.
(55) Chiou, B. S.; Khan, S. A. *Macromolecules* **1997**, *30*, 7322–7328.
(56) Cook, W. D. *Polymer* **1992**, *33*, 600–609.
(57) Gasper, S. M.; Schissel, D. N.; Baker, L. S.; Smith, D. L.; Youngman, R. E.; Wu, L.-M.; Sonner, S. M.; Hancock, R. R.; Hogue, C. L.; Givens, S. R. *Macromolecules* **2006**, *39*, 2126–2136.
(58) Schwalm, R. *UV coatings Basic, Recent Developments and New Application*, 1st ed.; Elsevier: Amsterdam, 2007; pp36−37.
(59) Sato, Y.; Fujiwara, K.; Takikawa, T.; Sumarno; Takishima, S.; Masuoka, H. *Fluid Phase Equilib*. **1999**, *162*, 261–276.
(60) Bird, R. B.; Stewart, W. E.; Lightfoot, E. N. *Transport Phenomena*, 2nd ed.; Wiley: New York, 2002; pp 300−303.